PNAS RESEARCH ARTICLE | APPLIED PHYSICAL SCIENCES OPEN ACCESS

# Coexistence of vitreous and crystalline phases of $H_2O$ at ambient temperature

Ali K. Shargh[a,1], Aude Picard[b,1], Rostislav Hrubiak[c,1], Dongzhou Zhang[d], Russell J. Hemley[e], Shanti Deemyad[f,2], Niaz Abdolrahim[a,2], and Saveez Saffarian[f,g,h,2]

Edited by Zachary Fisk, University of California, Irvine, Irvine, CA; received September 20, 2021; accepted May 18, 2022

**Formation of vitreous ice during rapid compression of water at room temperature is important for biology and the study of biological systems. Here, we show that Raman spectra of rapidly compressed water at greater than 1 GPa at room temperature exhibits the signature of high-density amorphous ice, whereas the X-ray diffraction (XRD) pattern is dominated by crystalline ice VI. To resolve this apparent contradiction, we used molecular dynamics simulations to calculate full vibrational spectra and diffraction patterns of mixtures of vitreous ice and ice VI, including embedded interfaces between the two phases. We show quantitatively that Raman spectra, which probe the local polarizability with respect to atomic displacements, are dominated by the vitreous phase, whereas a small amount of the crystalline component is readily apparent by XRD. The results of our combined experimental and theoretical studies have implications for detecting vitreous phases of water, survival of biological systems under extreme conditions, and biological imaging. The results provide additional insight into the stable and metastable phases of $H_2O$ as a function of pressure and temperature, as well as of other materials undergoing pressure-induced amorphization and other metastable transitions.**

water | HDA | ice VI

## Significance

Understanding the phase behavior of $H_2O$ is essential in geoscience, extreme biology, biological imaging, chemistry, and physics. Vitreous phases of $H_2O$ are of particular importance since these phases avoid the typical expansion of $H_2O$ during ice-crystal formation. Here, we confirm the existence of vitreous ice and ice VI in mixed-phase samples of $H_2O$ at room temperature and high pressure. We show how Raman scattering and X-ray diffraction alone lead to misleading characterization and understanding of the mixed-phase material, a conclusion supported by molecular dynamics simulations. The coexistence of vitreous and crystalline components of $H_2O$ under these conditions is crucial for experimental studies of biological systems. The results have implications for related metastable transitions in other materials under pressure.

Life as we know it on Earth depends on water. However, water also poses a critical challenge to life when it freezes at atmospheric pressure and low temperatures. The crystallization of $H_2O$ to form hexagonal ice (ice $I_h$) under these conditions is accompanied by its well-known expansion, which has a dramatic impact on the structure and function of living cells. This crystallization of $H_2O$ disrupts biological membranes and intracellular organization in living organisms and also displaces and concentrates salts and nutrients in the space between crystals (1). Like many liquids, however, rapid cooling of $H_2O$ at ambient pressure to below its glass-transition temperature results in the formation of an amorphous phase known as low-density amorphous ice. Amorphous solid $H_2O$ provides a chance for biological functions to survive where life otherwise cannot exist. Low-density amorphous ice is not the only amorphous form of $H_2O$. Ice $I_h$ transforms to high-density amorphous (HDA) ice by application of ∼1 GPa of pressure at temperatures below 130 K (2, 3). In addition, a distinct, very-high-density amorphous state (vHDA) can form by isobaric heating and cooling of the HDA (4). low-density amorphous, high-density amorphous, and very-high-density amorphous state ice thus represent the three dominant, solid amorphous forms of $H_2O$ at low temperatures.

Solid amorphous phases of $H_2O$ are broadly important in biology and biological applications. That amorphous $H_2O$ which can exist over a broad range of temperatures, from cryogenic conditions to room temperature, is particularly interesting in the context of biological systems. Managing ice crystals is vital for extremophiles to survive damaging effects of $H_2O$ crystallization. These organisms inhibit the growth of ice crystals and regulate the size and shape of the crystals using special antifreeze proteins (5, 6). Additionally, amorphous phases of $H_2O$ are important in preserving biological samples in cryotomography applications. In cryotomography, the amorphous $H_2O$ at low temperature is utilized routinely for sample preparation (7, 8), and significant efforts have been devoted to increase information obtained from cryotomography techniques. The low-temperature regime of amorphous $H_2O$ routinely accessed in cryotomography creates challenges for light microscopy due to freezing of index-matching medium and objectives, which result in lowering the resolution of light microscopy in these applications. Room-temperature amorphous phases of $H_2O$ are, therefore, advantageous for light microscopy applications and further development of techniques such as correlative light and electron microscopy (9–11).

While formation of amorphous phases of $H_2O$ below 200 K has been reported in many studies (2, 3, 12–16), a particularly interesting result is the observation of the Raman signature of HDA ice during fast compression of water at room temperature

Author contributions: S.D. and S.S. designed research; A.K.S., A.P., R.H., D.Z., S.D., N.A., and S.S. performed research; S.D., N.A., and S.S. contributed new reagents/analytic tools; A.K.S., A.P., S.D., N.A., and S.S. analyzed data; and A.K.S., R.J.H., S.D., N.A., and S.S. wrote the paper.

The authors declare no competing interest.

This article is a PNAS Direct Submission.



[1]A.K.S., A.P., and R.H. contributed equally to this work.

[2]To whom correspondence may be addressed. Email: Saffarian@physics.utah.edu or Niaz@rochester.edu or Deemyad@physics.utah.edu.

This article contains supporting information online at http://www.pnas.org/lookup/suppl/doi:10.1073/pnas.2117281119/-/DCSupplemental.

Published June 28, 2022.

and moderate pressures (17). On the other hand, independent X-ray diffraction (XRD) measurements of $H_2O$ on fast compression could not verify the formation of amorphous $H_2O$ above 200 K (18). Here, we report high-resolution micro-Raman and synchrotron XRD measurements conducted in parallel in rapidly compressed samples of water in diamond anvil cells (DACs). Our findings, that are supported by molecular dynamics simulations, shed light on the nature of the HDA ice at room temperature and reconciled conflicting previous reports.

## Results

**X-ray and Raman Measurements.** Experiments were performed using a piezo-driven dynamic-DAC (dDAC) capable of fast dynamic compression and decompression of materials (19). Initially, we established the criteria to create HDA based on Raman and visual observations. Samples of water loaded in the dDAC, were subject to compression by application of step-function voltage to dDAC resulting in compression rates of >0.25 TPa/s, as shown in Fig. 1 and detailed in *SI Appendix*. Decompression was also achieved through step-function application; it was previously reported that decompression rates do not affect the observed phases of $H_2O$ (17). Various paths of compression and decompression, as shown in Table 1, were examined and once the system reached a pressure plateau, $H_2O$ was monitored by Raman and optical imaging. Raman spectra clearly show the established transitions and signatures of different phases of the $H_2O$: liquid water, ice VI, ice VII, and HDA, as well as mixed phases in different regions consistent with findings from previous studies (3, 17) (Fig. 1 and Table 1). Upon pressurization of water to form HDA, the O–H symmetric-stretch mode shift to lower wavelength and the sample becomes transparent, indicative of the complete transformation to the amorphous form, as in previous DAC studies (3, 16).

Experiments were then performed in which both XRD and Raman spectra from the same sample were measured. Following path D in Table 1, we pressurized water to 1.7 GPa. Fig. 2 shows the sequence of Raman and XRD measurements at 1.7 GPa. Raman spectra collected both prior to and after XRD measurements indicated the presence of pure and homogenous HDA (Fig. 2 *A* and *B*). We subsequently collected and spatially resolved the XRD patterns on the sample throughout mapping the entire sample area (Fig. 2 *C* and *D*). Whereas the Raman data and visual observations (Fig. 2 *A* and *B*) repeatedly indicated the HDA phase throughout the sample, the XRD results consistently indicated ice VI and no observed amorphous background (Fig. 2 *C*, *D*, *G*, and *H*). On the other hand, the Raman spectra of HDA were observed through the sample, as shown in Fig. 2 *E* and *F*. It is notable that both XRD and Raman data were collected using similar spot sizes of ~10 $\mu m^2$ and, in both cases, repeating the measurements throughout the sample area gave the same results.

Moreover, a sample of $H_2O$ was pressurized up to 2.7 GPa, following the sequence illustrated in Fig. 2, and only was characterized using XRD. XRD of this sample up to 2.7 GPa (Fig. 3) displayed only the signature of either ice VI or ice VII, depending on pressure conditions, whereas Raman spectroscopy and visual observation indicated the presence of ice VI, VII, and HDA, as well as mixed phases at different pressures (Fig. 1). In addition, no indication of HDA was detected by XRD at room temperature up to 3 GPa. We also followed a different path, path E in Table 1, and prepared $H_2O$ at 1.7 GPa. Interestingly, XRD captured ice VI as the active phase

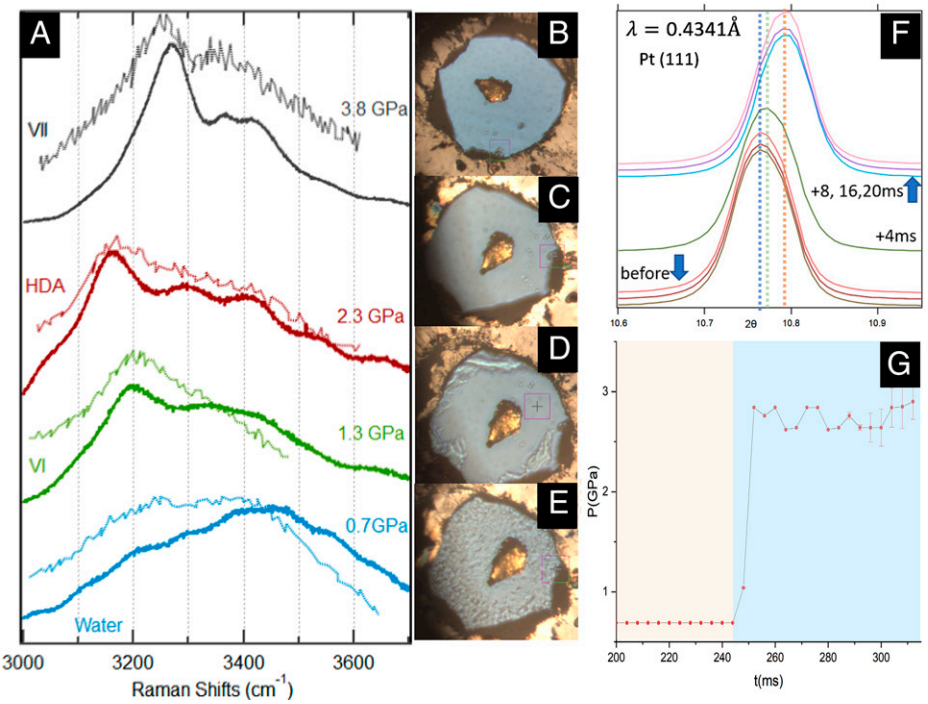


**Fig. 1.** Raman spectra and optical images of samples of water subjected to fast compression at room temperature in a dDAC. More specifically, referring to Table 1, ice VII is prepared following path A, ice HDA and liquid water are prepared following path B, and ice VI is prepared using path C. The intermediate phases of $H_2O$ are also reported in paths B and C. (*A*) Raman spectra. Solid lines are spectra collected in this study at the indicated pressures and the dotted lines are spectra reported in ref. 17. (*B*–*E*) Transmitted light images of the samples corresponding to the Raman spectra in *A*; that is, (*B*) pure ice VII, (*C*) pure HDA, (*D*) mixed HDA, and ice VI (HDA in center and ice VI at the edges), and (*E*) pure ice VI. The chip of gold (Au) used for pressure determination is evident at the center of the sample. We note that spectra from ref. 17. were collected at slightly different pressures: 0.6 GPa for water, 1.1 GPa for ice VI, 1.5 GPa for HDA, and 3.2 GPa for ice VII. (*F*) Measurement of the response time of dDAC based on the shift of Pt (111) Bragg peak under fast compression. (*G*) Time evolution of the pressure. Pink-shaded area represents the pressure before the voltage pulse. Rapid rise after voltage application shows a compression rate of >0.25 TPa/s.

**Table 1. Different path sequences used in this study.**

| Path | Experiments | Path sequence (phase and method) |
|---|---|---|
| A | Raman and optical | 0 GPa → 3.8 GPa (VII) |
| B | Raman and optical | 0 GPa → 2.3 GPa (HDA + VII phase separated) → 2.16 (HDA + VII phase separated) → 1.8 (HDA) → 0.7 (liquid water) |
| C | Raman and optical | 0 GPa → 2.26 GPa (VII + HDA phase separated) → 1 GPa (VI + liquid water phase separated) → 1.3 GPa (VI) |
| D | Raman and optical plus XRD | 0 GPa → 1.7 GPa (Raman: HDA XRD: VI) → 2.2 GPa (Raman: VII + HDA phase separated XRD: VII + VI) → 2.7 GPa (Raman: VII XRD: VII) |
| E | XRD | 0 GPa → 0.8 GPa (liquid water) → 2.6 GPa (VII) → 1.0 GPa (liquid water) → 1.7 GPa (VI) |

The phase of the sample at the end of each transformation and the detection method are shown.

of $H_2O$, similar to the observation from path D. This finding verifies that the characterized phase of $H_2O$ at 1.7 GPa is independent of the phase-transformation sequence.

Another notable observation is the change in average grain size observed in these experiments. Fig. 3 shows XRD images of different phases of ice collected at room temperature. The number of spots per ring at each pressure can be used to estimate the average size of the grains based on the focused X-ray–spot size. For the same X-ray spot on the sample, the average grain size is lower when HDA is present compared with that of pure ice VI. In the region where both Raman and XRD suggest ice VI (Fig. 3*A*), we estimate the average grain size to be ∼2 to 3 μm. However, in the region where Raman suggests HDA (Fig. 3*B*), we obtained a smaller grain size of ∼0.5 to 1 μm. The observation of ice VI at 1.7 GPa indicates the coexistence of ice VI and HDA. The smaller grain size of ice VI at 1.7 GPa compared with 0.75 GPa would result in a larger amount of interface between HDA and ice VI phases (see Molecular Dynamics Simulations section). We also note that in the ice VII region (Fig. 3*C*), the sample is powder-like, with very small grain sizes relative to the X-ray beam.

These results suggest that XRD is sensitive to the total volume fraction of ice VI, whereas the Raman measurements fail to capture ice VI if the grain size is small and the interface

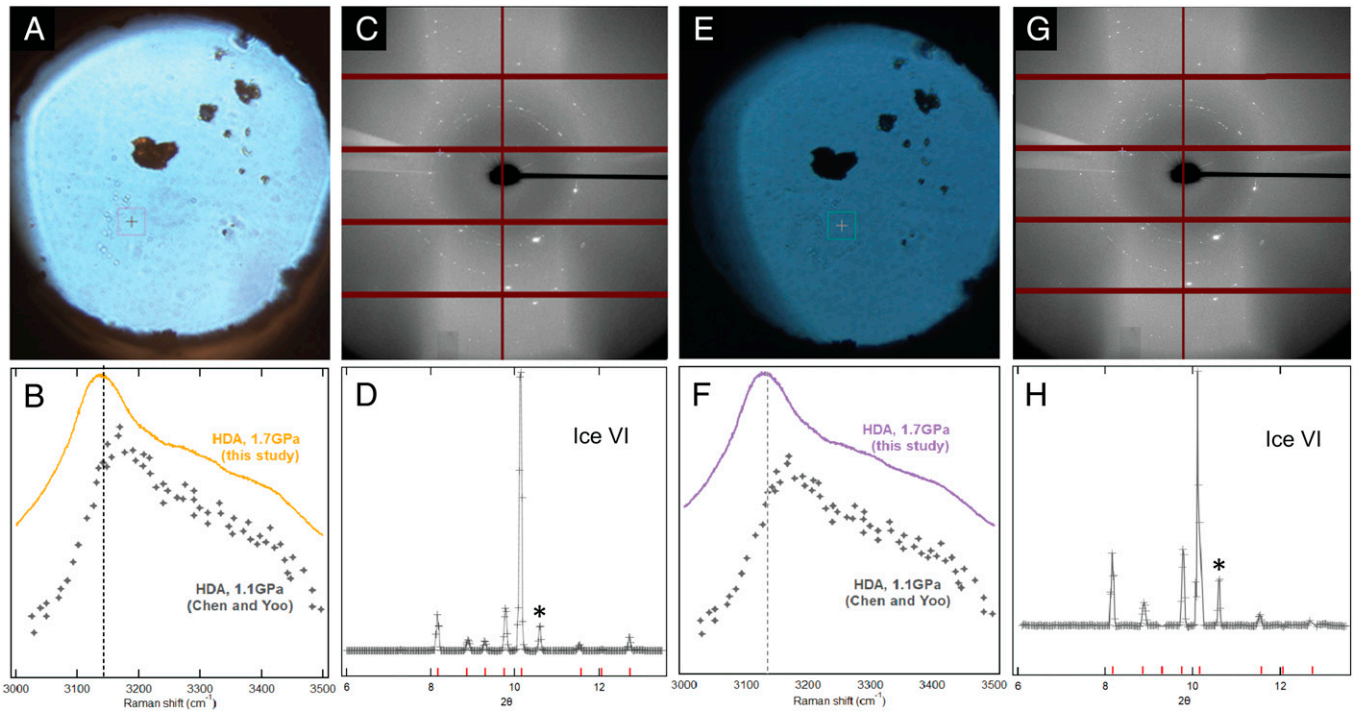


**Fig. 2.** Selected optical micrographs, Raman spectra, and XRD patterns from an $H_2O$ sample at 1.7 GPa and room temperature prepared following path D in Table 1. (*Left* to *Right*) The *Top* and *Bottom* panels represent the time sequence of each measurement. (*A* and *B*) Optical image and Raman spectra of the sample at the beginning of the measurements. (*C* and *D*) XRD image plate and integrated Bragg peaks from the sample collected, consistent with ice VI. The asterisks show a peak from the gold (Au) pressure calibrant. (*E* and *F*) Optical image and Raman spectra of the sample after the XRD. (*G* and *H*) Repeated XRD image plate and the Bragg peaks of the sample collected after the second Raman measurement, still consistent with ice VI. All data within the panels were acquired from the same sample in <1 h. The citation of Chen and Yoo refers to ref. 17.

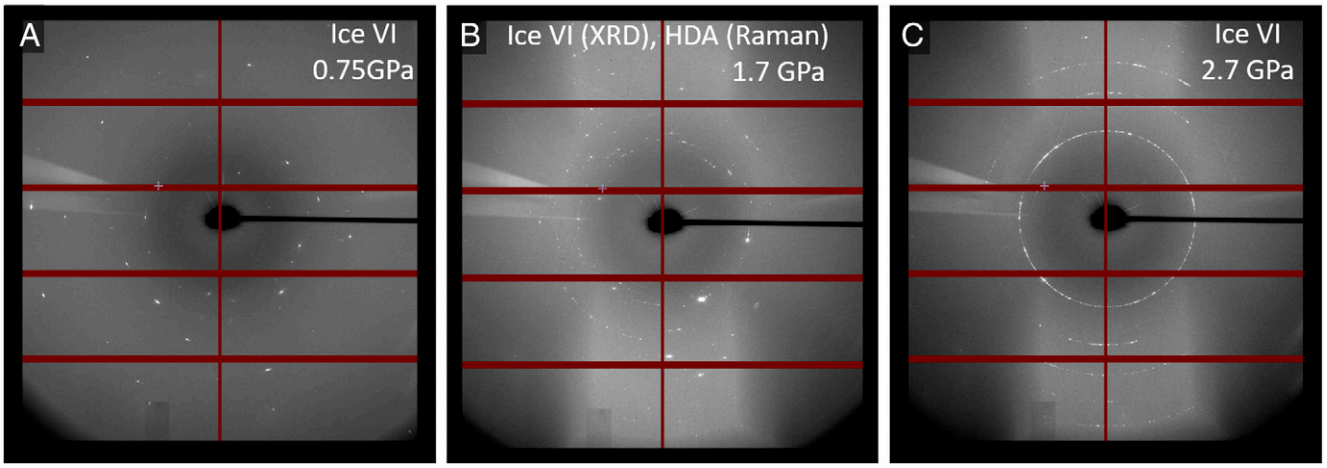


**Fig. 3.** Selected XRD image-plate measurements of an $H_2O$ sample at different pressures and room temperature during a single experiment. (*A*) Ice VI, also observed by Raman. (*B*) Ice VI; Raman spectroscopy measured once before and once after XRD on the same sample showed HDA, moving the dDAC between Raman to XRD and back to Raman took ~30 min, during which no change in Raman spectra was detected. (*C*) Ice VII, also observed by Raman scattering.

volume between ice VI and HDA is large. In order to further test this hypothesis, we modeled the ice VI/HDA system via simulations, as described in the next section.

**Molecular Dynamics Simulations.** We used molecular dynamics (MD) simulations to investigate ice VI and HDA phases of $H_2O$, generating both XRD patterns and vibrational spectra from different models of the coexisting phases. MD simulation is a powerful computational technique that has been extensively used to study the structural behavior of materials with different microstructures at the nanoscale (20–26). The application of the MD technique to phases of $H_2O$, including amorphous phases, has a long history (27–34). Moreover, numerous tests of intermolecular potentials, including those based on the TIP4P model, have been examined, performed and calibrated against data from $H_2O$ as a function of pressure and temperature (25, 35–37). Such MD simulations have also been used to study the coexistence of multiple phases of $H_2O$, including vapor, high-density ice, and liquid on the surface of carbon nanotubes at ambient conditions (24), where, it was concluded, nanometer confinement of water is the key for explaining such coexistence at these conditions. MD simulations have also been used to study the effect of density on the infrared (IR) spectrum of supercritical water (26).

In our MD simulations, we modeled the coexistence with a sandwich structure using three different values of initial phase volume fraction, including $\frac{N_{VI}}{N_{HDA}} = \frac{1}{3}$, 1, and 3, where $N_{VI}$ and $N_{HDA}$ are the numbers of molecules in ice VI and HDA phases, respectively (Fig. 4 *A*–*C*). In addition, we designed an embedded coexistence model with initial $\frac{N_{VI}}{N_{HDA}}$ ~3 but with three different volumes of the interface, to investigate the effects of interface volume on the XRD pattern and vibrational spectra (Fig. 4 *D*–*F*). All our coexistence models can be separated into three different regions: bulk ice VI, bulk ice HDA, and an interfacial region that is partially amorphous (Fig. 4), using established techniques to separate the regions (38–40). Here, it is useful to note that an increase in the volume of interfacial region (Fig. 4 *D*–*F*) is equivalent to a continuous decrease in the ice VI grain size, analogous to the mixed-phase system with small grain size. We calculated both IR and Raman vibrational spectra from the simulations. While both IR and Raman spectra generated with MD simulations captured the peak splitting as the main difference between the vibrational spectra of ice VI and HDA, such peak splitting was more distinct in IR spectra from the MD simulations (*SI Appendix*). Additional results of MD simulations of the XRD pattern and vibrational spectra of pure ice VI and HDA phases are discussed in the *SI Appendix* and are further used to compare the coexistence models in detail. Due to limitation of the interatomic potential used (35), the temperature in the MD simulations was kept at 225 K.

**Vibrational Spectroscopy of Sandwich Coexistence Model.** XRD, Raman, as well as IR spectra of coexistence sandwich models are shown in Fig. 5. As observed from MD simulations of pure ice VI and HDA, XRD of ice VI has several sharp peaks, while XRD of pure HDA resembles a Gaussian distribution with one broad peak (*SI Appendix*). The XRD patterns calculated from all three models include several sharp peaks, while only the model with $\frac{N_{VI}}{N_{HDA}} = \frac{1}{3}$ has broadened peaks (Fig. 5 *A*–*C*). Comparison of the results of the sandwich coexistence model and pure phases shows that the signature of ice VI is traceable in XRD of all three coexistence models, while the presence of HDA is only captured in the XRD of the model with $\frac{N_{VI}}{N_{HDA}} = \frac{1}{3}$ (i.e., $N_{HDA} > N_{VI}$), in which the peaks are significantly broadened. The MD simulations thus indicate that XRD is not able to readily capture the presence of HDA when its phase volume fraction is smaller than that of ice VI (Fig. 5 *B* and *C*). This is consistent with the conclusion discussed in the X-ray and Raman Measurment section based on our initial experimental XRD measurements.

The MD-generated Raman spectra (Fig. 5 *G* and *H*) imply that the spectra of two models with $\frac{N_{VI}}{N_{HDA}} = \frac{1}{3}$ and $\frac{N_{VI}}{N_{HDA}} = 1$ resemble a broad asymmetric distribution toward higher frequencies (similar to the Raman spectra of pure HDA shown in *SI Appendix*), whereas a sharp peak at lower frequency and a shoulder at higher frequency are captured in the Raman spectra of the model with $\frac{N_{VI}}{N_{HDA}} = \frac{3}{1}$ (similar to the Raman spectra of pure ice VI shown in *SI Appendix*) (Fig. 5*I*). The calculated IR spectra are presented in Fig. 5 *D*–*F*, and the MD-generated IR spectra for pure HDA and ice VI are shown in the *SI Appendix*. Fig. 5 *D* and *E* shows that the spectra of $\frac{N_{VI}}{N_{HDA}} = \frac{1}{3}$ and of $\frac{N_{VI}}{N_{HDA}} = 1$ exhibit a broad asymmetric distribution toward lower frequencies (similar to pure HDA shown in *SI Appendix*), while Fig. 5*F* shows that two distinct sharp peaks are clearly predicted in the IR spectra of the model with $\frac{N_{VI}}{N_{HDA}} = \frac{3}{1}$ (similar to pure ice VI shown in *SI*

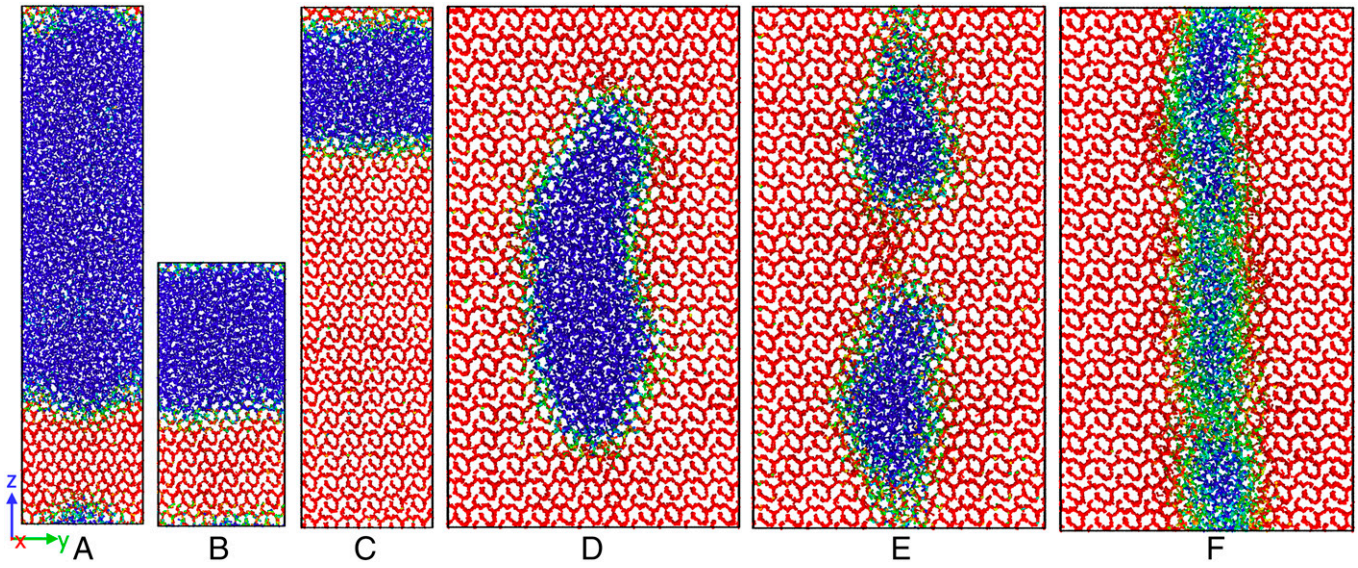


**Fig. 4.** Modeling volume fraction and interface effects of HDA and ice VI in MD simulations. (*A–C*) Ice VI and HDA sandwich systems with different initial phase volume fraction of (*A*) $\frac{N_{VI}}{N_{HDA}} = \frac{1}{3}$ (*B*) $\frac{N_{VI}}{N_{HDA}} = 1$, and (*C*) $\frac{N_{VI}}{N_{HDA}} = \frac{3}{1}$. (*D–F*) Ice VI and HDA–embedded systems with initial $\frac{N_{VI}}{N_{HDA}} = 2.23$ and with increasing interface volume, from left to right. Ice VI, ice HDA, and the interfacial regions are distinguished by red, blue, and green, respectively.

*Appendix*). These observations imply that the signature of ice VI is only present in the IR and Raman spectra of the coexistence model with $\frac{N_{VI}}{N_{HDA}} = 3$, while the IR and Raman spectra of the other two models mainly show HDA.

The MD simulations, therefore, show that, in contrast to XRD, vibrational spectra can only identify ice VI when its phase volume fraction is noticeably larger than that of HDA. In other words, the XRD pattern is much more sensitive to the ice VI volume fraction of our coexistence models. This can be better understood by comparing the maximum peak intensity of the patterns of pure ice VI and HDA (*SI Appendix*, Table S1). The maximum peak intensity of pure ice VI in XRD is 5.3 times higher than the corresponding value of pure HDA, while the ratio is 1.8 and 1.5 for IR and Raman, respectively. Therefore, in the ice VI–HDA mixed-phase system, the ice VI component governs the maximum peak intensity and the approximate shape of the XRD pattern.

These observations confirm our hypothesis that phase volume fraction of the mixed phase plays a key role in traceability of each constituent phase in XRD as well as vibrational spectra. In relative terms, XRD is not sensitive to the presence of HDA in the ice VI and HDA coexistence model unless the amount of HDA is significantly greater than that of ice VI (i.e., $N_{HDA} \geq 3N_{VI}$), while the IR/Raman spectrum is less sensitive to the presence of ice VI unless ice VI is significantly greater than HDA (i.e., $N_{VI} \geq 3N_{HDA}$). The results of the MD simulations could further explain our initial experimental observations in which the Raman spectra show HDA while XRD only reveals ice VI (e.g., Fig. 2). For instance, the experimental observation would be a coexisting ice VI and HDA with large grains in which the volume of ice VI is smaller than that of HDA (i.e., $\frac{N_{VI}}{N_{HDA}} \leq 1$) and the ice VI phase is only detected by XRD, not Raman. This scenario is consistent with the experimental observations shown in Fig. 2, yet it fails to describe the small grains observed in Fig. 3.

**Vibrational Spectroscopy of the Embedded Coexistence Model.** As described in the previous section, when the volume fraction of ice VI is about three times larger than HDA in the coexistence model with $\frac{N_{VI}}{N_{HDA}} = 3$, both XRD and IR/Raman spectra of MD simulations identify the presence of the ice VI (Fig. 5 *C*, *F* and *I*). While we do not know the exact phase volume fraction in experimental systems, we speculate that the "interface volume" is another important parameter that could play a role in understanding the different effects measured between XRD and Raman spectroscopy of $H_2O$ in these experiments. This means that increasing the volume of interfaces between ice VI and HDA and keeping phase volume fractions constant (i.e., $\frac{N_{VI}}{N_{HDA}} = 3$), might still result in XRD with no sign of HDA and vibrational spectra that cannot identify ice VI. Thus, we also investigated the effects of interface volume on XRD as well as vibrational spectra of coexistence models with $\frac{N_{VI}}{N_{HDA}} \sim 3$ and with different interfacial volume. For this investigation, we used the embedded coexistence model, because the arrangement enabled us to introduce higher interface volume into the system while keeping the phase volume fraction constant. Three embedded structures with different values of interface volumes of 37.9, 50.6, and 71.5 $nm^3$ were generated following the steps described in the *SI Appendix*.

The XRD patterns and vibrational spectra calculated from these models are shown in Fig. 6. The XRD results from all three models are relatively similar to each other and include several sharp peaks (Fig. 6 *A–C*). This indicates that XRD of all three models identifies ice VI as the major component, and further increase in interface volume does not substantially affect the XRD. Here, the peaks in XRD are broader in the embedded model (Fig. 6 *A–C*) compared with the sandwich model (Fig. 5 *C*) for the same volume fraction of $\frac{N_{VI}}{N_{HDA}} = 3$. This result suggests that the peak broadening is due to the large interface volume in the embedded structure.

Inspection of the calculated IR spectra (i.e., the smoothed curves in Fig. 6 *D–F*) reveals the valley between the two peaks tends to develop with an increase in the interface volume. With increasing interface volume, the IR spectrum continuously changes from that characterized by two peaks (similar to ice VI) to a broad feature with an asymmetry toward lower frequencies (similar to HDA ice). The results consistently show ice VI as the dominant phase. In addition, the calculated Raman spectrum (Fig. 6 *G–I*) evolves from that featuring a peak at lower frequency and a shoulder at higher frequency (similar to pure ice VI) to one with broad band with an asymmetry toward higher frequencies (similar to HDA ice). We cannot further increase the interface

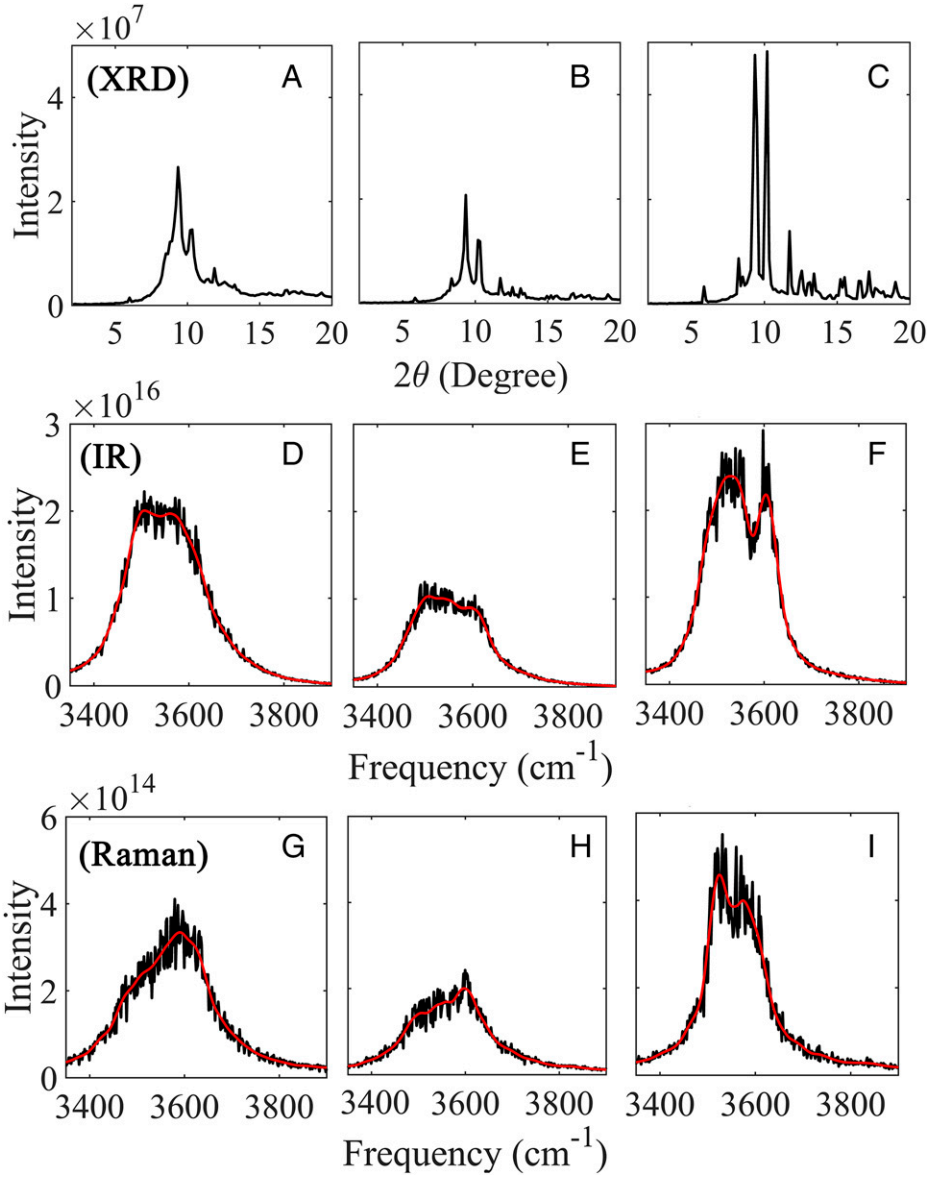


**Fig. 5.** XRD and IR/Raman spectra from MD simulations. (*A*–*C*) XRD and (*D*–*F*) IR, and (*G*–*I*) Raman spectra of sandwich coexistence model systems with (*A, D,* and *G*) $\frac{N_{VI}}{N_{HDA}} = \frac{1}{3}$, (*B, E,* and *H*) $\frac{N_{VI}}{N_{HDA}} = 1$, and (*C, F,* and *I*) $\frac{N_{VI}}{N_{HDA}} = \frac{3}{1}$. Intensities are given in arbitrary units.

volume to distinctly observe such a transition in IR/Raman spectra, due to size limitations of our MD simulations. However, such observation shows that in addition to the phase volume fraction, interface volume is another parameter that affects the measurable vibrational spectrum of the phases in coexistence. Therefore, a second scenario for explaining the apparent inconsistency in the experimental observations would be an ice VI and HDA mixed-phase system with $\frac{N_{VI}}{N_{HDA}} > 1$, in which numerous, small ice VI grains are in contact with the HDA regions. The results further indicate that fine-grain ice VI is not readily detected by Raman spectroscopy, due to the large volume of the interface between the two phases. Given the evidence for small grains of ice VI in the mixed-phase samples studied by diffraction and spectroscopy, the second scenario from the MD simulations is in qualitative agreement with the experiment (e.g., Figs. 2 and 3*B*).

## Discussion

Previous measurements of water under rapid compression at room temperature with XRD and Raman spectroscopy revealed an apparent inconsistency between the results of the two methods. Using both techniques, together with simulation, we resolved the issue. A major implication of our study is, thus, the importance of performing parallel XRD and spectroscopy measurements in identification of amorphous phases of water. As shown in our MD simulations, the spectroscopic method can have significant dependence of interface volume of mixed phases, while XRD does not show such a dependency. Our combined simulation and experimental strategies reveal that in the region between stability field of ice VI and ice VII, ice can coexist as HDA and ice VI with small grains.

The present results for ice are closely analogous to the in situ observations of pressure-induced amorphization and formation of coexisting crystalline-amorphous phases of other materials on compression at room temperature. Kingma et al. (41) found that such amorphization of $\alpha$-quartz is a gradual transformation that begins with formation of planar defects followed by growth of amorphous lamellae along those defects, producing heterogeneous samples of coexisting crystalline and amorphous phases.

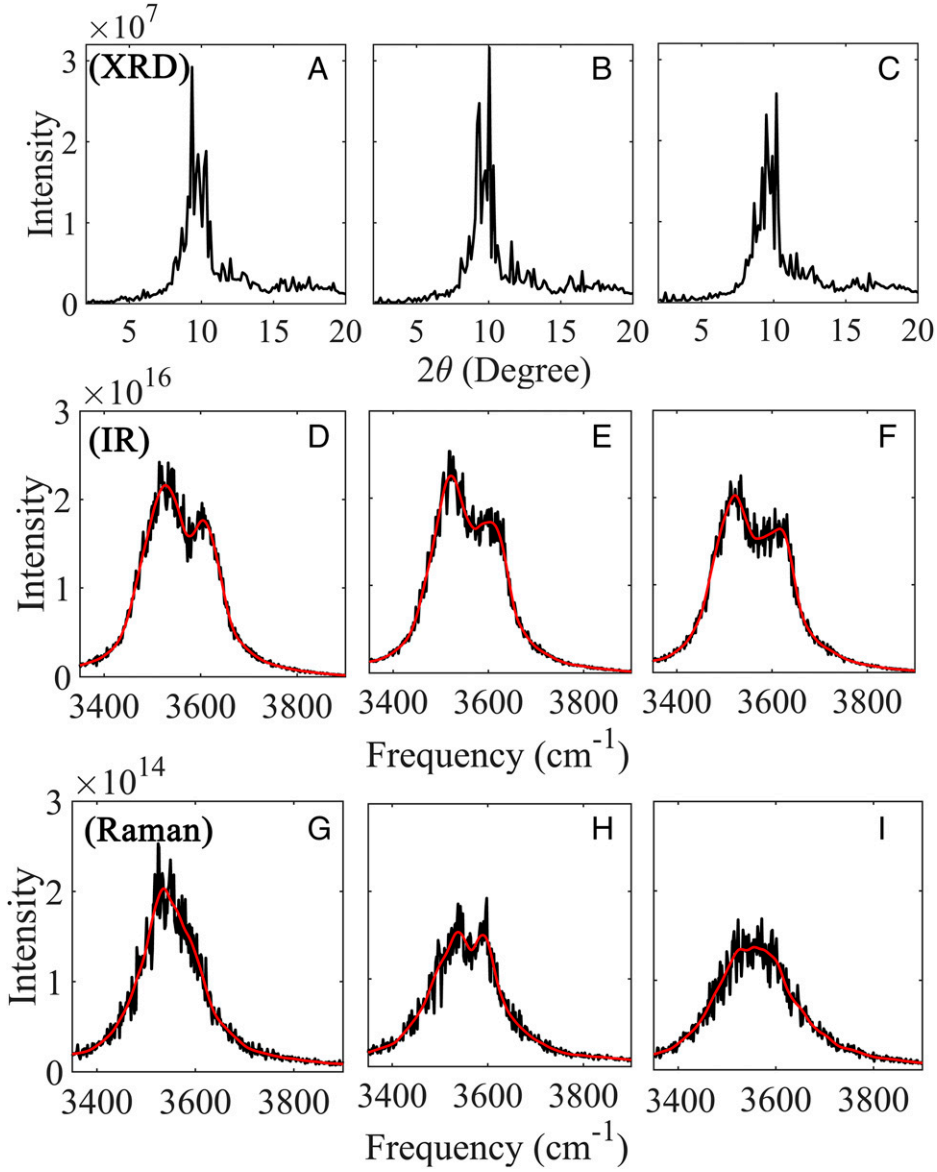


**Fig. 6.** Simulated (*A–C*) XRD, (*D–F*) IR, and (*G–I*) Raman spectra from the embedded coexistence model with $\frac{N_{VI}}{N_{HDA}}$ = 2.23, where the interface volume is 37.9, 50.6, and 71.5 nm$^3$, respectively, from left to right in each row. Intensities are given in arbitrary units.

Such high-pressure amorphization has also been found in other silica polymorphs such as coesite (42) and cristobalite (43), and other materials under static as well as shock loading (44).

The nucleation of new phases of ice within supercooled $H_2O$ is a topic of continuing great interest (3, 4, 45, 46)). Hemley et al. (3) identified the formation of ice VI, ice VII, and potentially other phases of $H_2O$ in coexistence with HDA ice at variable pressure and temperature conditions below ambient temperature. In that study, various transformation mechanisms between phases were also proposed (3), including the instability model analogous to that identified previously for α-quartz (42) and later examined in MD simulations of low-temperature, pressure-induced amorphization of ice $I_h$ (28). The transition from HDA to a form of ice VII near 4 GPa at low temperature that had been predicted by early MD simulations (27) was also identified (3). In the present room-temperature study, we did not resolve the mechanism of formation of the HDA–ice VI mixed-phase system at these conditions, but our results are not inconsistent with the earlier work. In our MD simulations, the average potential energy per molecule of pure ice VI and pure HDA at 1.5 GPa are calculated as −0.52 eV and −0.49 eV, respectively. Such close average potential energies imply that the coexistence of ice VI and HDA is energetically favorable. In addition, our calculations indicate that ice VII cannot be stabilized at 1.5 GPa and room temperature; thus the coexistence of ice VII and ice HDA at 1.5 GPa would be unlikely at the conditions studied experimentally here.

Our observations have important ramifications for survival of biological systems under extreme conditions (1, 5, 6, 47), as well as for biological imaging using approaches such as cryotomography (7, 8). Major questions, however, remain as to whether the structure of the biological membranes can survive in these conditions. Specifically, it remains to be investigated whether the small ice VI crystals present in the mixed HDA and ice VI region threaten the integrity of biological systems. Current evidence suggests that the mixed HDA and ice VI composite is only accessed by passing through the pure ice VI region (17), which would be detrimental to integrity of the biological systems. A separate route to this region of the phase diagram away from ice VI would be essential for biological structures to survive in this mixed-phase region.

## Methods

The experiments were performed using a dynamic-DAC using piezo control (19), with estimated compression rates between 0.05 TPa/s and 1 TPa/s and stainless-steel gaskets. Gold was used for pressure determination. Raman spectra were collected using the confocal micro-Raman system at GeoSoilEnviroCARS (GSECARS), Sector 13 of the Advanced Photon Source, Argonne National Laboratory, in the forward-scattering geometry with 1200 g/mm grating. A 532-nm laser was used for excitation at low power. The XRD was measured at beamline 13-BM-C at GSECARS. An X-ray wavelength of 0.4341 Å was used, and the data were collected by using a PILATUS3 1M (Dectris) detector. The X-ray beam was focused to a size of $\sim 10\ \mu m^2$ using a Kirkpatrick–Baez mirror. The exposure time for XRD was set to 4 s/frame.

Details of the structure generation and MD simulations are explained in the *SI Appendix*. To separate interfacial regions and calculate the volume of interface, we used the algorithms Coordination Analysis (38) as well as Construct Surface Mesh (39), implemented in OVITO (40).

**Data Availability.** All study data are included in the article and/or supporting information.

**ACKNOWLEDGMENTS.** The authors acknowledge V. B. Prakapenka for fruitful discussions and guidance in performing the measurements, and Y. J. Ryu for help with the Raman measurements. This research was partially supported by NIH Grant R01 AI150474 (to S.S.); a University of Utah seed grant (to S.D.), US Department of Energy (DOE), Office of Science (SC); and Fusion Energy Sciences, under Award Number DE-SC0020340 (to S.D., N.A., and R.H.). The high-pressure single and powder X-ray diffraction experiments were performed at 13-BM-C of GeoSoilEnviroCARS (GSECARS) of the University of Chicago, which is located at Sector 13 at the Advanced Photon Source (APS), Argonne National Laboratory (ANL). GSECARS is supported by the NSF Division of Earth Sciences (Grant EAR-1634415) and DOE-SC Basic Energy Sciences (BES; Grant DE-FG02-94ER14466). 13-BM-C is partially supported by NSF (Consortium for Materials Properties Research in Earth Sciences, Grant EAR-1661511). Work at ANL (sample preparation and crystal growth) is supported by the US DOE, Office of Basic Energy Science, Materials Science and Engineering Division. Use of the APS at ANL was supported by the DOE-SC-BES under Contract No. DE-AC02-06CH11357. Computational resources were provided by the Center for Integrated Research Computing at University of Rochester. We acknowledge HPCAT (Sector 16), APS, ANL, for providing the dDAC and supporting equipment for conducting the measurements. HPCAT operations are supported by DOE National Nuclear Security Administration (NNSA), Office of Experimental Sciences. The APS is a DOE User Facility operated for the DOE-SC by ANL under Contract No. DE-AC02-06CH11357. A.P. is supported by a Nevada NASA Experimental Program to Stimulate Competitive Research, Research Infrastructure Development seed grant. R.H. acknowledges support from the NSF (DMR-2104881) and the DOE NNSA through the Chicago/DOE Alliance Center (Grant DE-NA0003975).

Author affiliations: [a]Department of Mechanical Engineering, University of Rochester, Rochester, NY 14627; [b]School of Life Sciences, University of Nevada Las Vegas, Las Vegas, NV 89119; [c]High Pressure Collaborative Access Team, X-ray Science Division, Argonne National Laboratory, Argonne, IL 60439; [d]Hawaii Institute of Geophysics and Planetology, University of Hawaii at Manoa, Honolulu, HI 96822; [e]Departments of Physics, Chemistry, and Earth and Environmental Sciences, University of Illinois Chicago, Chicago, IL 60607; [f]Department of Physics and Astronomy, University of Utah, Salt Lake City, UT 84112; [g]Center for Cell and Genome Science, University of Utah, Salt Lake City, UT 84112; and [h]School of Biological Sciences, University of Utah, Salt Lake City, UT 84112

1. B. Wowk, Thermodynamic aspects of vitrification. *Cryobiology* **60**, 11–22 (2010).
2. O. Mishima, L. D. Calvert, E. Whalley, 'Melting ice' I at 77 K and 10 kbar: A new method of making amorphous solids. *Nature* **310**, 393–395 (1984).
3. R. J. Hemley, L. C. Chen, H. K. Mao, New transformations between crystalline and amorphous ice. *Nature* **338**, 638–640 (1989).
4. T. Loerting, C. Salzmann, I. Kohl, E. Mayer, A. Hallbrucker, A second distinct structural "state" of high-density amorphous ice at 77 K and 1 bar. *Phys. Chem. Chem. Phys.* **3**, 5355–5357 (2001).
5. J. S. H. Lorv, D. R. Rose, B. R. Glick, Bacterial ice crystal controlling proteins. *Scientifica (Cairo)* **2014**, 976895 (2014).
6. P. G. Debenedetti, *Metastable Liquids* (Princeton University Press, 1997).
7. J. Dubochet *et al.*, Cryo-electron microscopy of vitrified specimens. *Q. Rev. Biophys.* **21**, 129–228 (1988).
8. E. I. Tocheva, Z. Li, G. J. Jensen, Electron cryotomography. *Cold Spring Harb. Perspect. Biol.* **2**, a003442 (2010).
9. M. Pedersen *et al.*, Correlative iPALM and SEM resolves virus cavity and Gag lattice defects in HIV virions. *Eur. Biophys. J.* **48**, 15–23 (2019).
10. B. G. Kopek *et al.*, Diverse protocols for correlative super-resolution fluorescence imaging and electron microscopy of chemically fixed samples. *Nat. Protoc.* **12**, 916–946 (2017).
11. K. A. Sochacki, G. Shtengel, S. B. van Engelenburg, H. F. Hess, J. W. Taraska, Correlative super-resolution fluorescence and metal-replica transmission electron microscopy. *Nat. Methods* **11**, 305–308 (2014).
12. H. Tanaka, A self-consistent phase diagram for supercooled water. *Nature* **380**, 328–330 (1996).
13. T. Loerting, N. Giovambattista, Amorphous ices: Experiments and numerical simulations. *J. Phys. Condens. Matter* **18**, R919–R977 (2006).
14. G. Malenkov, Liquid water and ices: Understanding the structure and physical properties. *J. Phys. Condens. Matter* **21**, 283101 (2009).
15. O. Mishima, K. Takemura, K. Aoki, Visual observations of the amorphous-amorphous transition in $H_2O$ under pressure. *Science* **254**, 406–408 (1991).
16. Y. P. Handa, O. Mishima, E. Whalley, High-density amorphous ice. III. Thermal properties. *J. Chem. Phys.* **84**, 2766–2770 (1986).
17. J.-Y. Chen, C.-S. Yoo, High density amorphous ice at room temperature. *Proc. Natl. Acad. Sci. U.S.A.* **108**, 7685–7688 (2011).
18. C. Lin, J. S. Smith, X. Liu, J. S. Tse, W. Yang, Venture into water's no man's land: Structural transformations of solid $H_2O$ under rapid compression and decompression. *Phys. Rev. Lett.* **121**, 225703 (2018).
19. W. J. Evans *et al.*, Dynamic diamond anvil cell (dDAC): A novel device for studying the dynamic-pressure properties of materials. *Rev. Sci. Instrum.* **78**, 073904 (2007).
20. A. Annamareddy, P. M. Voyles, J. Perepezko, D. Morgan, Mechanisms of bulk and surface diffusion in metallic glasses determined from molecular dynamics simulations. *Acta Mater.* **209**, 116794 (2021).
21. A. K. Shargh, G. R.Madejski, J. L. McGrath, N. Abdolrahim, Mechanical properties and deformation mechanisms of amorphous nanoporous silicon nitride membranes via combined atomistic simulations and experiments. *Acta Mater.* 222, 117451 (2022).
22. A. K. Shargh, G. R. Madejski, J. L. McGrath, N. Abdolrahim, Molecular dynamics simulations of brittle to ductile transition in failure mechanism of silicon nitride nanoporous membranes. *Mater. Today Commun.* **25**, 101657 (2020).
23. Y. Shimizu, T. Kurokawa, H. Arai, H. Washizu, Higher-order structure of polymer melt described by persistent homology. *Sci. Rep.* **11**, 2274 (2021).
24. A. Barati Farimani, N. R. Aluru, Existence of multiple phases of water at nanotube interfaces. *J. Phys. Chem. C* **120**, 23763–23771 (2016).
25. Q. Guo, M. R. Ghaani, P. K. Nandi, N. J. English, Pressure-induced densification of ice $I_h$ under triaxial mechanical compression: Dissociation versus retention of crystallinity for intermediate states in atomistic and coarse-grained water models. *J. Phys. Chem. Lett.* **9**, 5267–5274 (2018).
26. N. J. Hestand, S. E. Strong, L. Shi, J. L. Skinner, Mid-IR spectroscopy of supercritical water: From dilute gas to dense fluid. *J. Chem. Phys.* **150**, 054505 (2019).
27. J. S. Tse, M. L. Klein, Pressure-induced phase transformations in ice. *Phys. Rev. Lett.* **58**, 1672–1675 (1987).
28. J. S. Tse, Mechanical instability in ice *Ih*. A mechanism for pressure-induced amorphization. *J. Chem. Phys.* **96**, 5482–5487 (1992).
29. P. H. Poole, F. Sciortino, U. Essmann, H. E. Stanley, Phase behaviour of metastable water. *Nature* **360**, 324–328 (1992).
30. A. Vegiri, S. V. Schevkunov, A molecular dynamics study of structural transitions in small water clusters in the presence of an external electric field. *J. Chem. Phys.* **115**, 4175–4185 (2001).
31. S. Habershon, T. E. Markland, D. E. Manolopoulos, Competing quantum effects in the dynamics of a flexible water model. *J. Chem. Phys.* **131**, 024501 (2009).
32. J. Chiu, F. W. Starr, N. Giovambattista, Pressure-induced transformations in computer simulations of glassy water. *J. Chem. Phys.* **139**, 184504 (2013).
33. S. Pipolo *et al.*, Navigating at will on the water phase diagram. *Phys. Rev. Lett.* **119**, 245701 (2017).
34. H. Tanaka, T. Yagasaki, M. Matsumoto, On the role of intermolecular vibrational motions for ice polymorphs. III. Mode characteristics associated with negative thermal expansion. *J. Chem. Phys.* **155**, 214502 (2021).
35. C. P. Herrero, R. Ramírez, High-density amorphous ice: A path-integral simulation. *J. Chem. Phys.* **137**, 104505 (2012).
36. S. Han, M. Y. Choi, P. Kumar, H. E. Stanley, Phase transitions in confined water nanofilms. *Nat. Phys.* **6**, 685–689 (2010).
37. M. Rossi, H. Liu, F. Paesani, J. Bowman, M. Ceriotti, Communication: On the consistency of approximate quantum dynamics simulation methods for vibrational spectra in the condensed phase. *J. Chem. Phys.* **141**, 181101 (2014).
38. J. L. Yarnell, M. J. Katz, R. G. Wenzel, S. H. Koenig, Structure factor and radial distribution function for liquid argon at 85 °K. *Phys. Rev. A* **7**, 2130–2144 (1973).
39. A. Stukowski, Computational analysis methods in atomistic modeling of crystals. *JOM* **66**, 399–407 (2014).
40. A. Stukowski, Visualization and analysis of atomistic simulation data with OVITO–the Open Visualization Tool. *Model. Simul. Mater. Sci. Eng.* **18**, 015012 (2009).
41. K. Kingma, C. Meade, R. J. Hemley, H. K. Mao, D. R. Veblen, Microstructural observations of α-quartz amorphization. *Science* **259**, 666–669 (1993).
42. R. J. Hemley, A. P. Jephcoat, H. K. Mao, L. C. Ming, M. H. Manghnani, Pressure-induced amorphization of crystalline silica. *Nature* **334**, 52–54 (1988).
43. A. J. Gratz, L. D. DeLoach, T. M. Clough, W. J. Nellis, Shock amorphization of cristobalite. *Science* **259**, 663–666 (1993).
44. S. M. Sharma, S. K. Sikka, Pressure induced amorphization of materials. *Prog. Mater. Sci.* **40**, 1–77 (1996).
45. P. G. Debenedetti, Supercooled and glassy water. *J. Phys. Condens. Matter* **15**, R1669–R1726 (2003).
46. J. C. Palmer, P. H. Poole, F. Sciortino, P. G. Debenedetti, Advances in computational studies of the liquid-liquid transition in water and water-like models. *Chem. Rev.* **118**, 9129–9151 (2018).
47. N. Ando *et al.*, The molecular basis for life in extreme environments. *Annu. Rev. Biophys.* **50**, 343–372 (2021).